International Journal of Hydrogen Energy 265 (2026) 156888

Contents lists available at ScienceDirect

International Journal of Hydrogen Energy

journal homepage: www.elsevier.com/locate/he

Hydrogen permeation and trapping in iron at sub-atmospheric partial pressures using a gas/electrochemical Devanathan–Stachurski cell

Tommaso Grossi [a,*], Valentina Colla [a], Fernanda Di Giorgio [b], Renzo Valentini [c]

[a] TeCIP Institute,Scuola Superiore Sant'Anna, Via Moruzzi 1, Pisa, 56124, Italy
[b] Dipharma Francis S.r.l., Italy
[c] Dipartimento di Ingegneria Civile e Industriale, Università di Pisa, Largo Lucio Lazzarino 1, Pisa, 56122, Italy

ARTICLE INFO

Keywords:
Hydrogen permeation
Sub-atmospheric
Devanathan–stachurski cell
ARMCO iron
Trapping
Sieverts' law

ABSTRACT

At near-atmospheric pressure, Devanathan–Stachurski (DS) permeation measurements operate near reversible-trap saturation, preventing separate identification of trapping parameters. We show that sub-atmospheric H_2 partial pressures (0.01 to 1.00 bar) allow the reversible-trap density N_r and a model-derived effective binding energy E_b to be jointly identified from multi-pressure data. Two advances enable this regime in a hybrid gas/electrochemical DS cell: (i) a flow-mixed Ar/H_2 inlet controlling partial pressure by mass-flow ratio, and (ii) an in-cell palladium electroplating procedure under real-time monitoring that suppresses blistering on thin ARMCO iron foils. Measured steady-state fluxes scale as the square root of partial pressure, validating Sieverts' law. The 6-pressure dataset is described by the Johnson model ($R^2 = 0.919$), yielding $N_r = 1.17 \cdot 10^{17}$ cm^{-3} and $E_b = 59.3$ kJ mol^{-1}, consistent with literature. Individual McNabb–Foster fits show larger parameter scatter, and a global McNabb–Foster fit sharing one trap-parameter set across all pressures provides an independent cross-validation of the Johnson result.

1. Introduction

Hydrogen-induced material degradation is among the oldest unresolved problems in metallurgy [1–9]. Six decades after Devanathan and Stachurski [10,11] placed the quantitative measurement of hydrogen transport in metals on its modern electrochemical footing, the question of which steel can safely tolerate which hydrogen environment is still answered case by case [12–15]. Extending the measurement technique to a wider range of hydrogen activities would improve both the scientific characterisation of trap populations and the relevance of permeation data to real service conditions, yet a systematic implementation has not been reported [12,16–18].

Hydrogen transport in ferrite is governed by lattice diffusion in competition with trapping at lattice imperfections [19–23]. Reversible traps (dislocation cores, low-angle grain boundaries, low-energy interfaces) capture and release hydrogen on the experimental time scale; irreversible traps (high-energy precipitate/matrix interfaces, microvoids, MnS particles) capture but do not release without thermal activation [24–29]. Both populations modulate the macroscopic permeation transient: trap filling extends the time lag, trap saturation makes the effective diffusivity pressure-dependent, and in equilibrium with a gaseous H_2 inlet the dissolved concentration at the entry face is set by Sieverts' law, $C_0 = K_S\sqrt{P_{H_2}}$, which fixes the driving force for the steady-state flux.

The standard probe of all of this is the Devanathan–Stachurski cell, in which one face of a thin metallic membrane is cathodically charged with hydrogen and the opposite face is oxidised potentiostatically so that the measured anodic current is proportional to the hydrogen flux [10,11,30,31]. The international standards [30,31] quantify hydrogen transport through an effective Fickian diffusivity, $D_{\text{eff}} = L^2/(6\,t_T)$, fitted to a single permeation transient at fixed cathodic charging conditions. At the comparatively high hydrogen activities of cathodic charging the reversible-trap population is largely saturated [12,32] and D_{eff} is self-consistent with Fick's law, but the underlying lattice diffusivity and trap parameters are conflated inside the single fitted prefactor: inverting the analytical Johnson time-lag formula for separate trap parameters becomes a stiff non-linear inverse problem with strongly correlated parameters [33].

Johnson's model (formalised in Section 2.4) describes reversible trapping through two dimensionless parameters: a trap-strength parameter α, set by the reversible-trap density and its capture/release kinetics, and a trap-occupancy parameter β, set by the inlet lattice hydrogen concentration and the same kinetics. Several authors have pointed out the analytical limitations of operating exclusively at saturation [12,16].

* Corresponding author.
E-mail address: tommaso.grossi@santannapisa.it (T. Grossi).

https://doi.org/10.1016/j.ijhydene.2026.156888
Received 14 June 2026; Received in revised form 21 July 2026; Accepted 1 August 2026
Available online 10 August 2026

Nomenclature

A	Exposed membrane area	cm^2
C	Local concentration of dissolved hydrogen in the lattice	$mol\,cm^{-3}$
C_0	Dissolved hydrogen concentration at the inlet face	$mol\,cm^{-3}$
D_{app}	Apparent diffusivity	$cm^2\,s^{-1}$
D_L	Lattice diffusivity	$cm^2\,s^{-1}$
E_b	Trap binding energy	$kJ\,mol^{-1}$
F	Faraday's constant	$96\,485\ C\,mol^{-1}$
i_∞	Steady-state exit current	A
J	Hydrogen flux density	$mol\,cm^{-2}\,s^{-1}$
J_∞	Steady-state hydrogen flux density	$mol\,cm^{-2}\,s^{-1}$
J_∞^{ref}	Steady-state hydrogen flux density at reference pressure	$mol\,cm^{-2}\,s^{-1}$
k_i	Irreversible trap capture rate constant	$cm^3\,s^{-1}$
k_r	Reversible trap capture rate constant	$cm^3\,s^{-1}$
K_S	Sieverts solubility constant	$mol\,cm^{-3}\,bar^{-1/2}$
L	Membrane thickness	cm
n	Fractional trap occupancy at the inlet surface	
N_i	Irreversible trap density	cm^{-3}
N_r	Reversible trap density	cm^{-3}
N_T	Total trap density	cm^{-3}
p	Reversible trap release rate constant	s^{-1}
P_{H_2}	Hydrogen partial pressure	bar
$P_{H_2}^{ref}$	Reference hydrogen partial pressure (1.00 bar)	bar
Q	Cumulative hydrogen permeation per unit area	$mol\,cm^{-2}$
t	Time	s
t_L	Lattice (Fickian) time lag	s
t_T	Time lag (loading)	s
$t_T^{(d)}$	Discharge time lag (unloading)	s
T	Temperature	°C
v	Reversible trap fractional occupancy (θ_r)	
w	Irreversible trap fractional occupancy (θ_i)	
x	Spatial coordinate through the membrane thickness	cm
X	Dimensionless spatial coordinate (x/L)	
α	Dimensionless reversible trap-strength parameter	
β	Dimensionless reversible trap-occupancy parameter	
β_1	Reversible trap-occupancy parameter at reference pressure	
η	Dimensionless parameter (C_0/N_i)	
κ	Dimensionless irreversible trapping parameter ($N_i k_i L^2/D_L$)	
λ	Dimensionless trapping rate parameter ($N_r k_r L^2/D_L$)	
μ	Dimensionless release rate parameter (pL^2/D_L)	
ξ	Dimensionless total hydrogen concentration (lattice + trapped)	
ρ	Dimensionless parameter (C_0/N_r)	
τ	Dimensionless time ($D_L t/L^2$)	
χ	Dimensionless lattice concentration (C/C_0)	
χ_{ss}	Dimensionless steady-state lattice concentration	

First, at near-atmospheric cathodic-charging activity the reversible-trap occupancy $n = \beta/(1+\beta)$ approaches unity [12,32] and the Johnson formula is poorly conditioned: small simultaneous adjustments of α and β leave t_T/t_L nearly unchanged, so the two parameters cannot be independently resolved from a single-pressure or near-saturation dataset [33]. Second, the Johnson analytical framework [32] is most informative in its low-occupancy limit: when reversible traps are far from full, β scales as $\sqrt{P_{H_2}}$ via the Sieverts inlet boundary condition $C_0 = K_S\sqrt{P_{H_2}}$, and the pressure dependence of t_T/t_L becomes a strong experimental constraint on the trap-strength parameter α taken separately from the lattice diffusivity D_L. Third, the sub-atmospheric regime, combined with a pure-H_2 pre-conditioning run that saturates the irreversible traps, isolates the reversible-trap contribution to the transient: the irreversible subpopulation is filled beforehand and held saturated, so the analysed curves report cleanly on the reversible population that controls reversible-trap-limited transport.

Exposing a specimen directly to a controlled H_2 atmosphere is a well-established charging route: gas-phase time-lag permeation has long been used to extract lattice diffusivity and solubility in iron and steel membranes [34], and more recent high-pressure gas-charging studies characterise hydrogen transport [17] or fatigue-crack-growth behaviour [18] in a hydrogen-gas environment. None of these, however, probe a trap-limited permeation transient in the sub-atmospheric partial-pressure regime itself—the regime the conditioning argument above requires.

Lowering the hydrogen activity on the inlet face of a permeation cell has been proposed analytically as a way out of the saturation-limited regime [12,16], but its direct gas-phase realisation is operationally inconvenient: it requires a vacuum chamber on the inlet face, careful management of leak rates, and a separate hydrogen pressure transducer. To the best of the authors' knowledge, a systematic sub-atmospheric permeation campaign of this kind has not previously been carried out in a Devanathan–Stachurski cell.

The present work provides a practical route into this regime. A constant pure-H_2 stream is diluted with an inert carrier and metred by flow ratio, so that sub-atmospheric partial pressures are reached without any vacuum-side hardware. This enables permeation transients to be recorded across two decades of P_{H_2} in a single apparatus and, in turn, to exploit the pressure dependence of the time lag: fitting the transients jointly over all measured pressures separates the trap-strength and trap-occupancy parameters α and β_1—and hence N_r and the effective binding energy E_b—which a single near-saturation transient cannot resolve. The multi-pressure time-lag inversion itself is due to Johnson [32,35]; the contribution here is the experimental implementation that makes it accessible on real permeation data. A second, practical obstacle is peculiar to the gas-phase/electrochemical hybrid configuration used here: the palladium catalyst layer required to dissociate H_2 on the inlet face is itself prone to blistering during plating, because in highly diffusive ferrites the hydrogen co-deposited with the Pd recombines in subsurface cavities and ruptures the foil before the catalytic layer is complete. We address this with the controlled in-cell electroplating procedure of Section 2.1, which throttles the plating current under real-time exit-current monitoring to suppress blistering during Pd deposition on the highly diffusive ferrite. In-cell electroplating under exit-current monitoring follows established practice in hydrogen-permeation sensor fabrication; here it is what makes the thin ARMCO foils useable in the gas/electrochemical hybrid cell.

We demonstrate this approach on cold-rolled ARMCO iron across two decades of P_{H_2}. The Ar/H_2 flow-mixed inlet places the membrane in equilibrium with hydrogen partial pressures from $P_{H_2} = 0.01$ bar to 1.00 bar in a single apparatus, and the multi-pressure global trap-parameter inversion recovers the reversible-trap density and effective binding energy from the combined dataset; the controlled palladium electroplating of Section 2.1 is what makes the thin-foil measurements possible in the first place. The imposed partial pressures are validated by an independent Sieverts consistency check against the expected $\sqrt{P_{H_2}}$ dependence of the steady-state flux. The resulting multi-pressure dataset is analysed using both the Johnson closed-form time-lag formula [32] and the McNabb–Foster numerical inverse problem [20], which are standard tools for this class of measurements; we apply the McNabb–Foster solver both per-curve and, additionally, in a global multi-pressure form that shares one reversible-trap parameter set across all pressures (Section 2.6). The Johnson formula in its full two-parameter form reproduces the time-lag versus partial-pressure trend with a log-time $R^2 = 0.919$ on all 6 measured pressures when the lattice diffusivity is fixed at its literature value, and the McNabb–Foster PDE solver reproduces each transient individually to within experimental noise. Through a flow-ratio partial-pressure control methodology that accesses sub-atmospheric regimes without vacuum-side hardware, we enable Johnson's multi-pressure time-lag inversion for real permeation data—extracting well-conditioned trap parameters on a ferrite across two decades of pressure. The Johnson and McNabb–Foster frameworks are used here in their published form.

2. Materials and methods

2.1. Specimens, surface preparation and apparatus

The material is a high-purity ARMCO iron strip (C, N < 50 ppm) cold-rolled to a 90% reduction in the laboratory, annealed at 720 °C for one hour and furnace-cooled, then ground with progressively finer SiC papers (P320, P500, P600) to a final thickness of $L = 0.012$ cm. The exposed area in the permeation cell is $A = 3.97$ cm^2 and all experiments are run at $T = 20$ °C. The grinding sequence leaves a shallow deformed layer at the surface. Single-pass grinding of medium-carbon steel produces a work-hardened layer of order a few to about ten micrometres deep [36]; the progressive multi-grit SiC sequence used here (finishing at P600) is gentler than that controlled single-pass machine grinding, so this figure is an upper bound, and even so the layer is at most a few percent of the $L = 0.012$ cm ($\approx$ 120 μm) thickness. Because the reported quantities are through-thickness, steady-state and time-lag transport properties rather than near-surface hardness or diffusivity, this thin layer does not control the extracted D_L or trap parameters: the transients remain sigmoidal at every pressure (Fig. 5) and the steady-state flux follows the Sieverts $\sqrt{P_{H_2}}$ law down to the lowest explored pressure ($R^2 = 0.999$, Fig. 4), as expected for bulk-diffusion-limited transport. Grinding-induced dislocations may nonetheless contribute to the reversible trap population, since dislocation cores are among the recognised reversible trap sites in α-Fe [26,37].

The exit face of the specimen is coated with palladium to catalyse the recombination of permeated atomic hydrogen and lower the surface impedance, following the standard practice of the electrochemical-permeation literature [11,38–40]. Conventional electroplating from a $Na_2[Pd(NO_2)_4]$ bath at 0.4 mA cm^{-2} in 0.2 N NaOH causes systematic blistering of the highly diffusive ARMCO substrate (observed in this work): the hydrogen co-deposited with the palladium recombines inside subsurface cavities and ruptures the foil before the catalytic layer is complete. We circumvent this failure mode with what we term *controlled* palladium electroplating, in which the plating is performed inside a Devanathan–Stachurski cell, with the electroplating bath on the cathodic side and a standard 0.1 N NaOH anodic compartment on the opposite side, and the exit current measured continuously. The plating current is throttled in real time to keep the exit current below the critical blistering threshold. With this procedure, blister-free Pd layers approximately 0.1 μm thick are obtained reproducibly. Fig. 1 contrasts the blistered surface obtained by conventional electroplating with the smooth Pd layer produced by the controlled procedure.

The permeation cell, shown in Fig. 2, is the hybrid Devanathan–Stachurski configuration introduced above. The inlet face is exposed to a continuously refreshed gas stream of pure H_2 (supplied by an HG200B electrolytic generator with a palladium-membrane purifier, purity greater than 99.999 99%, dew point below −40 °C) diluted with high-purity argon from a commercial bottle. Flow ratio is set with two MKS 179 A/1179 A thermal mass-flow controller pairs (range 2%–100% of 500 sccm full scale, ±1% relative precision each). The two metred streams are combined at a junction upstream of the cell inlet and mix in a 1 m length of capillary-bore stainless-steel tubing (of the type used for gas-chromatograph connections, 1 mm internal diameter) before reaching the gas chamber. This corresponds to a tube volume of 0.79 cm^3 and, across the full documented flow range of the mass-flow controllers (10–500 sccm total), an axial residence time of 0.1–5 s—already negligible next to the duration of permeation runs (Section 3.1). Radial homogenisation across the 1 mm bore is even faster: with a Fuller–Schettler–Giddings estimate of the H_2/Ar binary diffusion coefficient, $D_{H_2-Ar} \approx 0.8$ cm^2 s^{-1} at $T = 20$ °C and 1 bar [41], the radial diffusion time $r^2/D_{H_2-Ar} \approx 3$ ms is 30–1500 times shorter than the axial residence time itself, depending on flow rate. Both gases are low-viscosity, single-phase streams at these flow rates, so no active mixing element beyond the junction and connecting line is required; the line is purged at the combined flow rate, so the inlet composition reaches steady state, and remains constant, before and during each measurement. The total gas pressure at the cell inlet is held at 1.00 bar; the H_2 partial pressure is the experimental control variable.

The exit (anodic) face is immersed in 0.1 N NaOH electrolyte and held at +200 mV versus the saturated calomel electrode by the potentiostat. The measured anodic current i is proportional to the hydrogen flux via $J = i\,(FA)^{-1}$. The total current error of the measurement chain is 40 nA ($\Delta J = 1.04 \cdot 10^{-13}$ mol cm^{-2} s^{-1}).

2.2. Metallographic characterisation

The crystalline microstructure of the as-tested XH01 foil was examined by optical microscopy and SEM after the 720 °C/1 h laboratory anneal. Specimens were hot-mounted in acrylic resin (Resth), mechanically ground with SiC papers of decreasing grit (P320 to P1200),

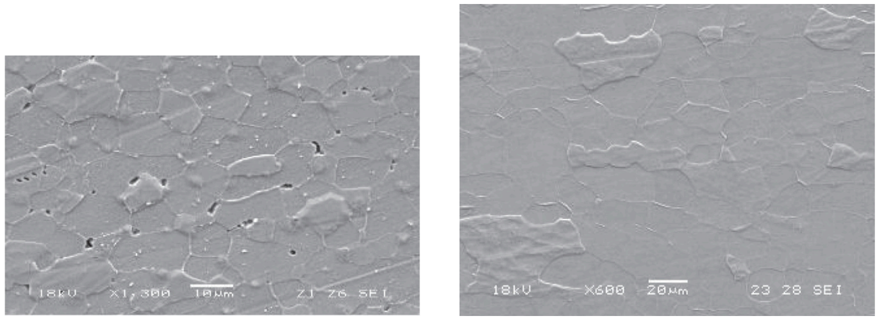

(a) (b)

Fig. 1. SEM micrographs of the palladium-coated ARMCO iron surface (cold-rolled ARMCO iron membrane, $L = 0.012$ cm, $T = 20$ °C). (a) Standard electroplating at 0.4 mA cm^{-2} in 0.2 N NaOH produces visible blisters caused by subsurface H_2 recombination. (b) The controlled in-cell procedure—where the plating current is throttled in real time to keep the exit current below the blistering threshold—yields a uniform, blister-free Pd layer.

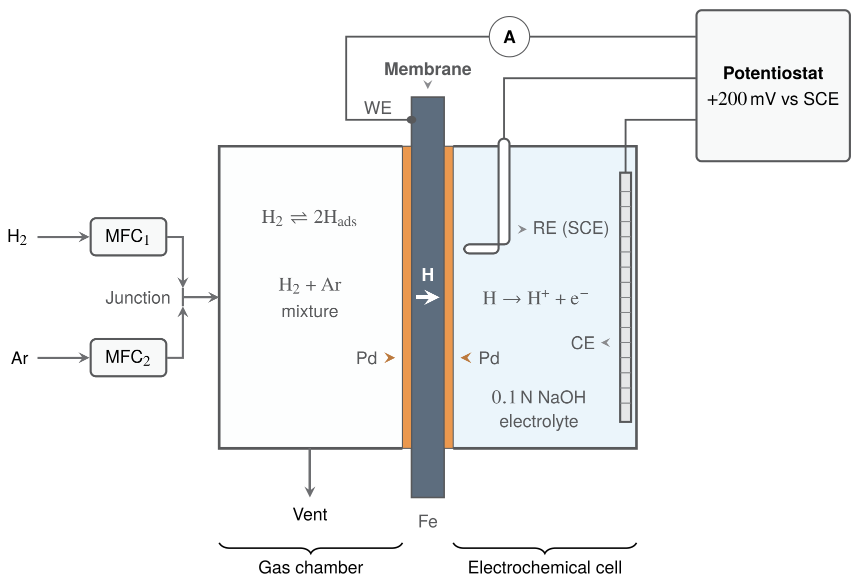

Fig. 2. Hybrid gas-inlet/electrochemical-outlet Devanathan–Stachurski permeation cell. Pure H_2 from an electrolytic generator is mixed with inert argon through two mass flow controllers (MFC_1, MFC_2). The resulting gas stream presses on the inlet face of the palladium-coated iron membrane (Fe); permeated atomic hydrogen (H) diffuses through the membrane and is oxidised at +200 mV vs the saturated calomel reference electrode (RE/SCE) in 0.1 N NaOH electrolyte. The exit current at the platinum counter electrode (CE) is proportional to the hydrogen flux and is recorded by the ammeter (A). *Abbreviations*: WE, working electrode (membrane, anodic face); RE, reference electrode; CE, counter electrode; SCE, saturated calomel electrode; MFC, mass flow controller; Pd, palladium catalyst coating; Fe, iron membrane. Cold-rolled ARMCO iron membrane: exposed area $A = 3.97$ cm^2, thickness $L = 0.012$ cm, held at $T = 20$ °C..

polished to a 1 µm diamond finish on a velvet lap, and etched for approximately 5 s in 2% Nital to reveal ferrite grain boundaries.

Fig. 3 shows representative optical (600×) and SEM (1200×, secondary-electron contrast) micrographs. Both images reveal equiaxed ferritic grains of 30–100 µm with well-defined grain boundaries and no observable second-phase particles. The small dark dots visible in the optical micrograph (Fig. 3(b)) are consistent with minor impurities within the ferrite matrix, revealed by the differential Nital-etch response; their composition was not further characterised. They are not resolved in the companion SEM micrograph of the same specimen (Fig. 3(a)), which shows clean grain interiors and boundaries at higher magnification: secondary-electron SEM imaging is primarily sensitive to surface topography rather than to the etch-chemistry contrast that reveals these features optically, so their absence from the SEM panel points to a compositional rather than topographic origin. The faint linear striations in Fig. 3(b) are, separately, residual polishing scratches from the SiC grinding sequence. Their sparse, isolated distribution and small size set them apart from a systematic second-phase population such as cementite or grain-boundary films, so they are not expected to form an additional trap population beyond the grain-boundary and dislocation sites discussed below. The equiaxed morphology indicates that the anneal substantially recrystallises the cold-rolled foil: the 90% cold-reduction dislocation substructure is not preserved at this magnification. The most prominent crystallographic defect resolved in this microstructure is the grain boundary; low-angle grain boundaries in particular are a recognised reversible trap site in α-Fe [26,37], whereas high-angle boundaries act as deeper, less reversible traps [26]. Alternative defect populations cannot be excluded. After severe cold reduction followed by annealing, residual defect structures such as vacancy clusters, collapsed dislocation debris, sub-micrometric microvoids, or semi-atomic-scale free-volume clusters may persist below the resolution of conventional optical and SEM observation, and may contribute to deep trapping together with grain boundaries. With no cementite particles, interfacial microvoids, or systematic second-phase population resolved at these magnifications (beyond the sparse, unidentified ferrite-matrix impurities noted above), the material is consistent with a single dominant reversible-trap population, as assumed by the Johnson model [32].

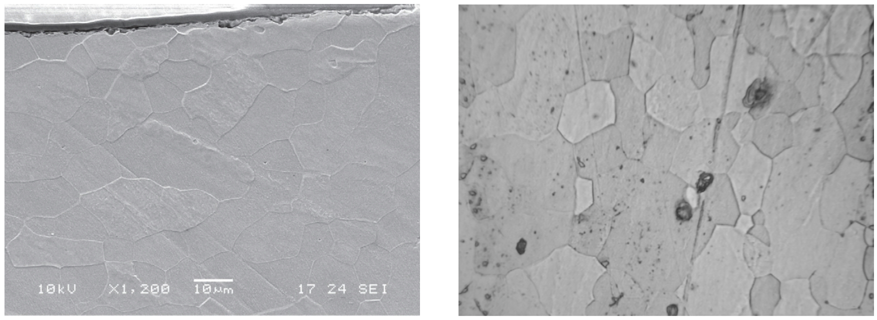

(a) (b)

Fig. 3. Metallographic characterisation of the as-tested XH01 foil (cold-rolled ARMCO iron, C, N < 50 ppm, L = 0.012 cm) after the 720 °C/1 h laboratory anneal. (a) SEM micrograph at 1200× (secondary-electron contrast). (b) Optical micrograph at 600× after 2% Nital etch; the scattered dark dots are consistent with minor, uncharacterised ferrite-matrix impurities revealed by etch contrast, and the faint linear striations are polishing scratches; neither is resolved in the higher-resolution, topography-sensitive SEM panel (a) — see main text. Both images show equiaxed ferritic grains of 30–100 µm with clean grain boundaries and no systematic second-phase population, consistent with a recrystallised high-purity α-Fe microstructure.

The membrane thickness ($L = 0.012$ cm $\approx$ 120 µm) is comparable to, and in places smaller than, individual grain diameters (30–100 µm), so a single line through the thickness traverses only a handful of grains. This has limited impact on the reported transport parameters. The exposed permeation area (A = 3.97 cm^2) is macroscopic and spans an estimated 10^4–10^5 grains laterally, so the measured flux and time lag are already an ensemble average over many grain orientations. Because interstitial hydrogen occupies tetrahedral sites in the cubic BCC lattice of α-Fe, whose macroscopic diffusivity tensor is isotropic by symmetry, the lattice diffusivity does not depend on grain orientation; only the orientation-independent trapping at grain boundaries and dislocations modulates the effective transport. The thin-foil geometry is a practical compromise—required to keep the permeation time lag tractable at the lowest explored pressures—and the reported parameters should be read as polycrystalline averages.

2.3. Pressure control and validation

The H_2 partial pressure inside the gas chamber is imposed experimentally by calibrated mass-flow control of the Ar/H_2 mixture: a constant pure-H_2 stream is blended with argon metred by the two MKS 179 A/1179 A thermal mass-flow controllers (±1% relative error each), so that the inlet partial pressure is set by the H_2/Ar flow ratio; the resulting pressure uncertainty is derived in Section 2.5. The nominal values used here span 0.01 to 1.00 bar.

The steady-state permeation flux additionally serves as an independent consistency check through the expected Sieverts-law dependence. At equilibrium with H_2 gas, the dissolved atomic-hydrogen concentration on the inlet face obeys Sieverts' law,

$$C_0 = K_S \sqrt{P_{\mathrm{H}_2}}, \tag{1}$$

where K_S is the Sieverts solubility constant of the matrix. For α-iron we adopt the Arrhenius expression of Johnson [32] (Eq. 9, p. 2377),

$$C_L = 1.57 \cdot 10^{20}\, P_{\mathrm{atm}}^{1/2} \exp\left(\frac{-6840\,\mathrm{cal\,mol^{-1}}}{RT}\right) \text{ atoms H cm}^{-3}, \tag{2}$$

which at T = 293 K and P_{H_2} = 1 bar yields $K_S = 1.24 \cdot 10^{15}$ atoms cm^{-3} bar$^{-1/2}$ (pressure unit converted from atm to bar), consistent with the Kiuchi–McLellan solubility data for α-Fe [29]. The steady-state hydrogen flux through a defect-free membrane is therefore proportional to $\sqrt{P_{\mathrm{H}_2}}$, so that the imposed pressures should satisfy

$$\frac{P_{\mathrm{H}_2}}{P_{\mathrm{H}_2}^{\mathrm{ref}}} = \left(\frac{J_\infty}{J_\infty^{\mathrm{ref}}}\right)^2 \tag{3}$$

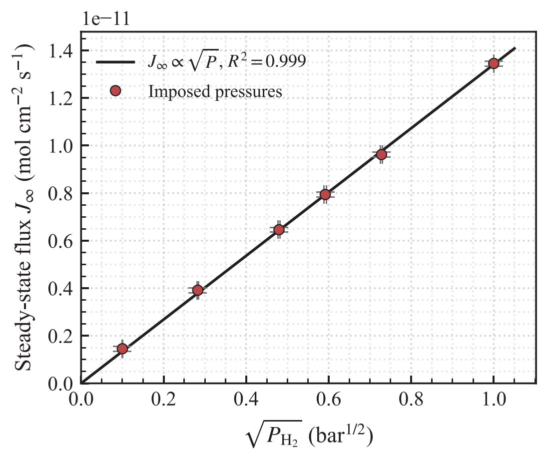

Fig. 4. Sieverts consistency check. Steady-state permeation flux J_∞ versus the square root of the imposed H_2 partial pressure for the six XH01 runs. The straight line through the origin is the one-parameter fit $J_\infty \propto \sqrt{P_{\mathrm{H}_2}}$ (R^2 = 0.999). Grey error bars denote the 1σ flow-calibration uncertainty on $\sqrt{P_{\mathrm{H}_2}}$ and the fixed current error Δi on J_∞; both are comparable to or smaller than the marker size.

relative to the pure-H_2 reference measurement at 1.00 bar. The measured fluxes follow this $\sqrt{P_{\mathrm{H}_2}}$ law closely (Fig. 4): a one-parameter fit $J_\infty \propto \sqrt{P_{\mathrm{H}_2}}$ over the imposed pressures gives R^2 = 0.999 and recovers an implied solubility within a factor of 1.12 of the literature K_S, confirming that the imposed partial pressures and measured fluxes are mutually coherent with Sieverts' law.

2.4. Time-lag analysis

The permeation transient $J(t)$ is integrated to give the cumulative permeation $Q(t) = \int_0^t J(t')\,\mathrm{d}t'$. At long times $Q(t)$ becomes linear in t with slope J_∞ and intercept on the time axis equal to the time lag t_T [42,43]. Johnson [32,35], generalising the pure-Fickian result $t_L = L^2/(6D_L)$, derived a closed-form expression for t_T in the presence of a saturating reversible-trap population in local equilibrium with the lattice. With two distinct dimensionless parameters,

$$\alpha = N_r \frac{k_r}{p}, \qquad \beta = C_0 \frac{k_r}{p} = \frac{n}{1-n}, \tag{4}$$

where N_r is the reversible-trap density, k_r and p are the trap capture and release rate constants and n is the fractional trap occupancy at the inlet surface, the time lag reads

$$\frac{t_T}{t_L} = 1 + \frac{3\alpha}{\beta} + \frac{6\alpha}{\beta^2} - \frac{6\alpha}{\beta^3}(1+\beta)\ln(1+\beta). \tag{5}$$

A derivation of Eq. (5) by the Frisch moment method [43] is given in Appendix. The same calculation applied to the *unloading* transient—inlet switched from C_0 to zero, inlet face exposed to pure argon—yields the identical formula, provided the time lag is redefined as $t_T^{(d)} = \int_0^\infty J(t)\,\mathrm{d}t \,/\, J_\infty$, i.e. the total hydrogen released per unit steady-state flux. In practice this requires integrating the full discharge curve to $t \to \infty$, which demands a complete discharge record; when only a partial record is available the loading transient remains the preferred route.

The trap-strength parameter α is intrinsic to the matrix at fixed temperature and the trap-occupancy parameter β scales as $\sqrt{P_{H_2}}$ through Eq. (1). In the empty-trap limit $\beta \to 0$, $n \to 0$, Eq. (5) reduces to $t_T = t_L(1+\alpha)$ (Oriani's effective-diffusivity limit [19]); in the saturated limit $\beta \to \infty$ it reduces to unity (pure lattice). We fix the lattice diffusivity at the literature value $D_L = 7.00 \cdot 10^{-5}$ cm^2 s^{-1} for α-Fe at $T = 20$ °C [29,32,44], and recover the two trap parameters ($\alpha, \beta_1 = \beta(P_{H_2} = 1.00$ bar)) by Trust-Region Reflective (TRF) least-squares minimisation [45] of the log-time-lag residual across all 6 pressures simultaneously in log-parameter space.

The inlet lattice concentration on the x-axis of the Johnson fit is evaluated from Sieverts' law as $C_0 = K_S\sqrt{P_{H_2}}$ using the literature K_S [32] and the imposed partial pressure. This is logically independent of the Sieverts consistency check of Section 2.3, which uses the *measured* steady-state flux to verify that the imposed pressures and the Sieverts $\sqrt{P}$ law are mutually coherent; the Johnson analysis uses K_S and the imposed P directly as input, without relying on the measured flux to determine C_0. Holding D_L at the literature value follows the convention of the original analysis and reflects the well-known degeneracy between D_L and the trap parameters in single-curve time-lag fitting [33].

Before evaluating Eq. (5), the steady-state flux J_∞ and time lag t_T are extracted from each raw current transient as follows. The plateau current is identified as the longest contiguous window over which the five-point moving average remains within 5% of the global maximum. The cumulative permeation $Q(t) = \int_0^t J\,\mathrm{d}t'$ is obtained by trapezoidal integration. The steady-state plateau is identified as the longest contiguous window over which the moving-average flux remains within 5% of its maximum. A linear regression of $Q(t)$ is then performed over a window starting at the onset of this plateau (where the flux first reaches 95% of the steady-state amplitude); this yields the time lag as the t-intercept of the asymptote.

2.5. Uncertainty propagation

Each of the 6 pressures was measured in a single permeation run. The uncertainties reported below therefore propagate from instrument calibration and measurement noise; no pressure-level replicates have been carried out. Two independent error sources contribute to the uncertainty on the fitted Johnson parameters. The current measurement chain carries a total error $\Delta i = 40$ nA, which propagates directly to the steady-state flux as $\Delta J = \Delta i\,(FA)^{-1} = 1.04 \cdot 10^{-13}$ mol cm^{-2} s^{-1}. The partial-pressure assignment depends on the ratio of two independent mass-flow controllers (one for H_2, one for Ar), each with a $\pm 1\%$ relative error ε. Since $P_{H_2} = P_{\mathrm{total}}\, Q_{H_2}/(Q_{H_2} + Q_{\mathrm{Ar}})$, standard propagation of independent relative errors gives

$$\sigma(P_{H_2}) = P_{H_2}\left(1 - \frac{P_{H_2}}{P_{\mathrm{total}}}\right)\varepsilon\sqrt{2}, \tag{6}$$

where $P_{\mathrm{total}} = 1$ bar is the total cell pressure. At $P_{H_2} = P_{\mathrm{total}}$ (pure H_2, Ar MFC inactive) $\sigma = 0$; as $P_{H_2} \to 0$ the relative uncertainty approaches $\varepsilon\sqrt{2} \approx 1.41\%$—slightly larger than the single-instrument 1%.

The central values and uncertainties on the Johnson parameters are obtained by Monte Carlo experiments: 1000 independent trials each perturb the raw current trace with Gaussian noise $\sigma_i = \Delta i$, draw perturbed pressures from Eq. (6), draw a single perturbed membrane thickness shared across all six pressures (see below), re-extract J_∞ and t_T, and refit Eq. (5). 998 of 1000 trials converged. We report the ensemble *mean* of each parameter as the central value—the expectation under the measurement-error model—with the 16th–84th percentiles as the 68% interval.

The membrane thickness L was measured with a manual mechanical micrometre (reading resolution 0.01 mm); following standard practice for manual instruments, we take the 1σ reading uncertainty as half the smallest graduation, $\sigma_L = 0.005$ mm (0.0005 cm, $\approx 4\%$ of L). L enters the Johnson time scale as $t_L = L^2/(6D_L)$, so a systematic thickness offset shifts the absolute time scale—and hence the fitted N_r and D_{eff}—proportionally. Because a single specimen (and hence a single micrometre reading) is common to all six pressures, we propagate σ_L by drawing one perturbed L per Monte Carlo trial, shared across all six curves, alongside the current and pressure perturbations above. This confirms the structural expectation quantitatively: a constant multiplicative shift in t_L is largely absorbed by the fitted α and cancels in the pressure dependence that determines the effective binding energy E_b, so including σ_L leaves the E_b uncertainty essentially unchanged ($\sigma(E_b) = 0.356$ kJ mol^{-1}, i.e. $\approx 0.6\%$ of the mean), while it dominates the uncertainty on the absolute reversible-trap density ($\sigma(N_r) = 1.01 \cdot 10^{16}$ cm^{-3}, i.e. $\approx 9\%$ of the mean, roughly six times larger than with only the current and pressure error sources). The reported N_r uncertainty above already includes the thickness contribution.

2.6. McNabb–Foster numerical model

The closed-form result of Eq. (5) assumes that all reversible traps share a single binding energy and that any irreversible-trap subpopulation is either absent or kinetically frozen on the time scale of the experiment. When these assumptions are violated, the full McNabb–Foster kinetic-trap system must be integrated numerically [20,24,46–48]. In dimensionless form, with $\chi = C/C_0$, $v = \theta_r$, $w = \theta_i$, $X = x/L$ and $\tau = D_L t/L^2$, the system is

$$\frac{\partial \chi}{\partial \tau} = \frac{\partial^2 \chi}{\partial X^2} - \lambda\chi(1-v) + \frac{\mu}{\rho}v - \kappa\chi(1-w), \tag{7}$$

$$\frac{\partial v}{\partial \tau} = \lambda\rho\,\chi(1-v) - \mu v, \tag{8}$$

$$\frac{\partial w}{\partial \tau} = \kappa\eta\,\chi(1-w), \tag{9}$$

with $\lambda = N_r k_r L^2/D_L$, $\mu = pL^2/D_L$, $\kappa = N_i k_i L^2/D_L$, $\rho = C_0/N_r$ and $\eta = C_0/N_i$. Note that the Johnson parameters satisfy $\alpha = \lambda/\mu$ and $\beta = \rho\lambda/\mu$, directly connecting the two parameterisations: in the limit $\kappa \to 0$ and under local trap equilibrium the MF system reduces to the Johnson framework.

The experimental protocol places the analysis squarely in this limit. Each specimen is first subjected to a pure-H_2 permeation at 1 bar that fills the irreversible (deep) traps; because these sites do not release hydrogen at room temperature, they remain saturated throughout the subsequent runs and act as inert, already-filled sinks rather than active traps. The permeation transients analysed here therefore carry information on the reversible trap population only, and we accordingly fit the reduced reversible system ($\kappa = 0$, i.e. Eqs. (7)–(8) with the irreversible term removed). In fact, the irreversible groupings are not identifiable from data that contain no irreversible-capture signal, and forcing them into the fit merely injects spurious scatter.

We solve the reduced system by the method of lines on 81 uniform spatial nodes with a second-order central-difference Laplacian and an implicit (backward-Euler) update with adaptive time stepping [45]. The inverse problem fits the three reversible dimensionless groupings (λ, μ, ρ) to each measured transient, with the lattice diffusivity held fixed at its literature value D_L (i.e. a fixed time scale L^2/D_L). The inverse problem is solved in two stages. In the first stage, a Bayesian

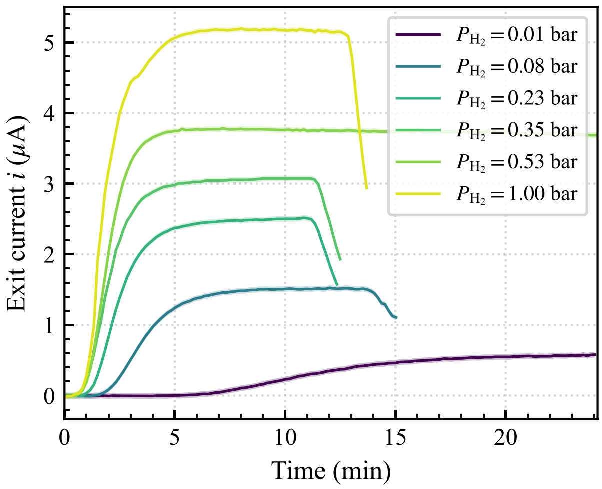

Fig. 5. Exit-current transients on cold-rolled ARMCO iron at the six explored H_2 partial pressures. The plateaux are well defined at every pressure.

global search using the Tree-structured Parzen Estimator (TPE) [49] algorithm as implemented in the Optuna framework [50] explores the log-parameter space within ±1 decade of an initial estimate derived from the plateau parameters, evaluating the RMS objective on a coarse spatial grid of 41 nodes (500 trials per curve, with 12 random start-up trials before the surrogate model takes over). In the second stage, the Bayesian optimum is refined by Nelder–Mead [51] simplex minimisation on the full 81-node grid (convergence criteria: $\Delta\theta < 10^{-3}$ and $\Delta f < 5 \cdot 10^{-4}$ in normalised parameter and residual space, respectively). The two-stage strategy is necessary because the RMS landscape has multiple local minima at the coarse resolution; the Bayesian phase provides a reliable basin-of-attraction estimate that Nelder–Mead then sharpens.

We should clearly distinguish curve reproduction from parameter identification. While high-dimensional numerical trapping models can reproduce individual permeation transients with close accuracy, a good fit alone does not guarantee uniquely identifiable transport parameters. The McNabb–Foster inverse problem is in fact strongly ill-conditioned [32,33,35]: widely separated parameter sets can give very similar fit quality for a single $J(t)$ curve, so that measurement noise projects onto correlated directions in parameter space. We therefore restrict the search to the three identifiable reversible groupings, hold D_L at its literature value, and report the fitted groupings rather than claiming uniquely determined dimensional values. All numerical values reported in the text and tables in Section 3.3 are derived from the raw current–time data through the procedures described above.

3. Results

3.1. Permeation transients and steady-state fluxes

Fig. 5 shows the six exit-current transients on ARMCO iron at the explored H_2 partial pressures (P_{H_2} = 0.01, 0.08, 0.23, 0.35, 0.53 and 1.00 bar). Each transient rises monotonically from a near-zero baseline to a well-defined plateau over a few minutes to one hour, followed by a smooth discharge phase once the gas-phase H_2 is replaced by pure argon. The well-defined plateaux indicate that the membrane reaches a steady state at every pressure. The signal at the lowest pressure ($P_{H_2} = 0.01$ bar) is approximately one order of magnitude smaller than the reference plateau but well above the noise floor of the potentiostat, indicating that the sub-atmospheric regime is operationally accessible.

The steady-state currents at the explored pressures, the corresponding hydrogen flux densities $J_\infty = i_\infty/(FA)$ and the time lags t_T

Table 1
Experimental characteristic quantities for cold-rolled ARMCO iron.

P_{H_2} (bar)	J_∞ (mol cm^{-2} s^{-1})	t_T (s)	D_{app} (cm^2 s^{-1})
0.01	$1.46 \cdot 10^{-12}$	677	$3.55 \cdot 10^{-8}$
0.08	$3.92 \cdot 10^{-12}$	223	$1.08 \cdot 10^{-7}$
0.23	$6.46 \cdot 10^{-12}$	153	$1.56 \cdot 10^{-7}$
0.35	$7.94 \cdot 10^{-12}$	125	$1.92 \cdot 10^{-7}$
0.53	$9.62 \cdot 10^{-12}$	123	$1.96 \cdot 10^{-7}$
1.00	$1.35 \cdot 10^{-11}$	121	$1.98 \cdot 10^{-7}$

extracted by the $Q(t)$-intercept method are summarised in Table 1. The apparent diffusivity $D_{app} = L^2/(6t_T)$ decreases from $1.98 \cdot 10^{-7}$ cm^2 s^{-1} at 1.00 bar to $3.55 \cdot 10^{-8}$ cm^2 s^{-1} at the lowest pressure, reflecting the influence of trap filling.

The extraction of the time lags t_T via the cumulative charge $Q(t)$-intercept method is illustrated in Fig. 6 for each of the six partial pressures. For each test run, the experimental cumulative permeation curve $Q(t) = \int_0^t J(t')dt'$ is plotted along with the fitted diagonal asymptote. The time axis intercept of this asymptote gives the time lag t_T, which represents the delay due to transient transport and trapping. The fitted asymptotes closely track the linear plateaux of the cumulative charge curves.

3.2. Johnson time-lag fit

Fig. 7 shows the time-lag ratio $(t_T/t_L) - 1$ versus the lattice concentration C_0 together with the two-parameter Johnson fit of Eq. (5), which illustrates the transition from the empty-trap regime to the trap-saturation limit. With the lattice diffusivity held at the literature value, the recovered trap parameters are

$$\alpha = 8.55 \cdot 10^3 \qquad (68\% \text{ CI: } 7.21 \cdot 10^3\text{–}9.84 \cdot 10^3), \tag{10}$$

$$\beta_1 = 91.1 \qquad (68\% \text{ CI: } 77.9\text{–}104), \tag{11}$$

reported as Monte Carlo ensemble means with 68% percentile intervals (Section 2.5); the Johnson form describes the 6 measured pressures with a best-fit log-time coefficient of determination $R^2 = 0.919$. The two parameters are then converted to physical quantities by eliminating the common ratio k_r/p between the definitions in Eq. (4). At the 1 bar reference, $C_0 = K_S\sqrt{1\text{ bar}} = K_S$, so $\beta_1 = K_S(k_r/p)$ and hence $k_r/p = \beta_1/K_S$. Substituting into $\alpha = N_r(k_r/p)$ gives the reversible-trap density directly,

$$N_r = \frac{\alpha}{k_r/p} = \frac{\alpha K_S}{\beta_1}, \tag{12}$$

with the Johnson Sieverts constant for α-Fe (from Eq. (2)). This yields $N_r = 1.17 \cdot 10^{17}$ cm^{-3} (68% CI: $1.07 \cdot 10^{17}$–$1.27 \cdot 10^{17}$ cm^{-3}) and a trap binding energy $E_b = 59.3$ kJ mol^{-1} (68% CI: 59.0–59.7 kJ mol^{-1}), derived via Oriani's equilibrium relation $E_b = RT\ln(k_r N_L/p)$ [19] with $N_L = 12/a_{Fe}^3 = 5.09 \cdot 10^{23}$ cm^{-3}, the tetrahedral interstitial site density in BCC α-Fe ($a_{Fe} = 2.8664$ Å). Both values agree well with Johnson [32] for cold-rolled iron and with Kumnick and Johnson [28] for deformed iron ($E_b = 59.9 \pm 4.6$ kJ mol^{-1}). Because the experiments were performed at a single temperature, this E_b should be regarded as a model-derived effective trapping energy—inferred through the Johnson/Oriani trapping framework from the pressure dependence at fixed T—rather than a direct Arrhenius measurement, which would require a temperature series (Section 4.1).

The residual panel of Fig. 7 quantifies the fitting quality across all six pressures: the relative deviation between observed and predicted time lag has an RMSE of 18.6%, with the single largest deviation occurring at the highest, reference pressure (P_{H_2} = 1.00 bar) rather than at the lowest. This pattern is consistent with the three Johnson-model assumptions discussed in Section 4.1: local equilibrium between lattice and trapped hydrogen, a single reversible-trap population, and

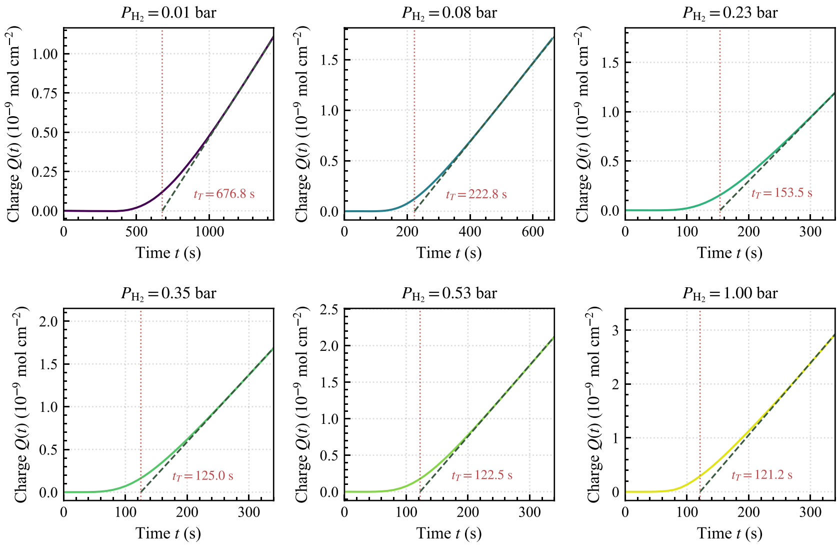

Fig. 6. Experimental cumulative permeation curves $Q(t)$ as a function of time t for the six explored H_2 partial pressures. The fitted diagonal asymptotes are shown as dashed lines, and their intercepts on the time axis mark the extracted time lags t_T (indicated by vertical dotted lines).

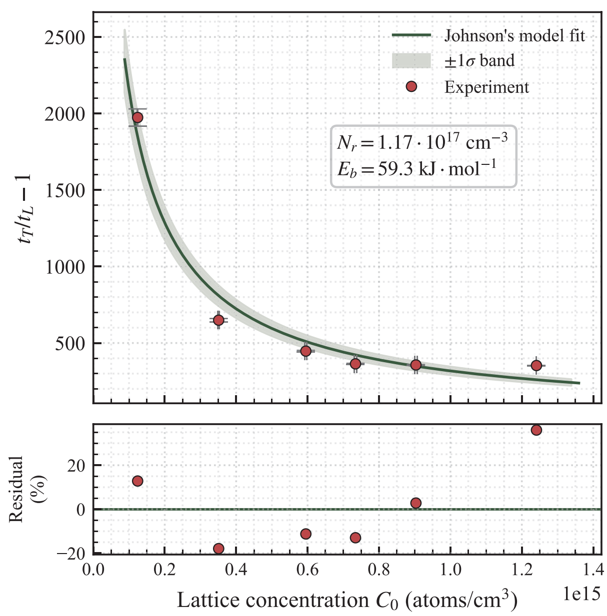

Fig. 7. Time-lag ratio $(t_T/t_L) - 1$ as a function of the lattice concentration C_0 for the six explored pressures, on cold-rolled ARMCO iron ($L = 0.012$ cm, $T = 20$ °C). The solid line is the two-parameter Johnson model (Eq. (5)) evaluated at the Monte Carlo mean parameters, with $D_L = 7.00 \cdot 10^{-5}$ cm^2 s^{-1} (fixed at the α-Fe literature value), implying a reversible-trap density $N_r = 1.17 \cdot 10^{17}$ cm^{-3} and a trap binding energy $E_b = 59.3$ kJ mol^{-1} as shown in the legend. The shaded band is the $\pm 1\sigma$ (16th–84th percentile) envelope of the Monte Carlo ensemble (Section 2.5); grey bars on the points are the propagated 1σ errors on C_0 and $(t_T/t_L) - 1$. The lower panel shows the relative fit residual, $(t_{T,\mathrm{obs}} - t_{T,\mathrm{pred}})/t_{T,\mathrm{pred}}$, at each pressure..

a fixed literature D_L. All three are most likely to be stressed where the trap occupancy $n = \beta/(1+\beta)$ is highest, i.e. near 1 bar. As occupancy saturates, trap release becomes rate-limiting; a distributed, rather than single-valued, trap-energy population [16,21] would manifest its curvature most strongly at saturation. The residual is therefore concentrated at high occupancy—a genuine limitation of the single-trap Johnson closed form—rather than a signature of a second trap population or a low-pressure noise artefact.

3.3. McNabb–Foster inverse fit

To evaluate the transport and trapping parameters under the McNabb–Foster (MF) kinetic-trap framework, we perform individual per-curve inverse fits on each of the six experimental transients separately, and, additionally, a single global fit that shares one reversible-trap parameter set (N_r, k_r, p) across all six transients simultaneously (Sections 2.6 and 3.3.2).

3.3.1. Single-pressure McNabb–Foster fits

Fig. 8 shows the individual MF fits for all six transients on a 2×3 grid. Experimental points carry $\pm 1.04 \cdot 10^{-13}$ mol cm^{-2} s^{-1} error bars normalised by J_∞; no fit band is shown because Nelder–Mead returns no covariance matrix and a full Monte Carlo ensemble of per-curve inverse fits would be computationally prohibitive. The numerical model reproduces the shape of each measured transient with high accuracy, achieving a maximum root-mean-square residual of 0.0184. The resulting parameters for each pressure are reported in Table 2. Even with the irreversible population removed, the per-curve reversible parameters

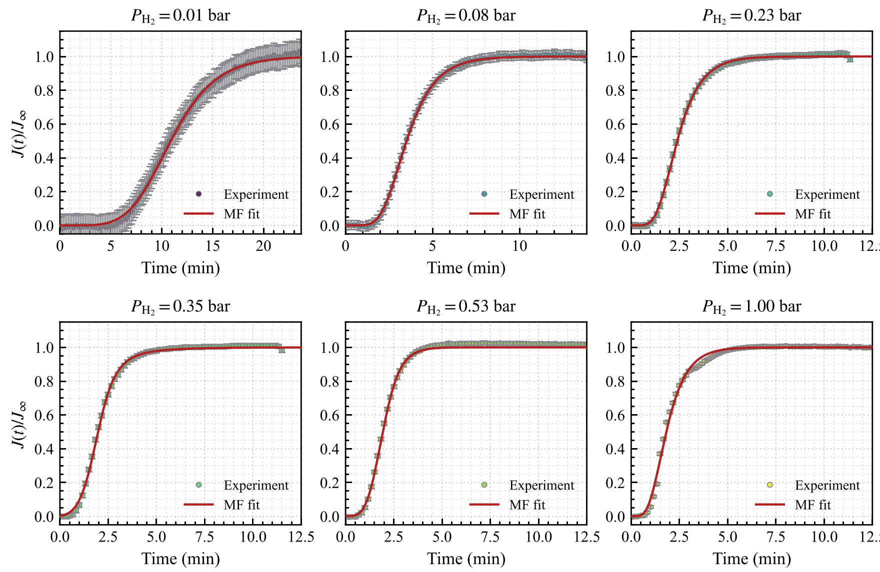

Fig. 8. McNabb–Foster individual inverse-fit overlays for the six ARMCO iron transients (cold-rolled ARMCO iron, L = 0.012 cm, T = 20 °C). Filled circles: experimental normalised flux. Solid line: individual MF fit with three independent parameters optimised per curve.

Table 2
Comparison of reversible-trap transport parameters identified by the global Johnson fit, the global McNabb–Foster fit (Section 3.3.2), and individual per-curve reversible-only McNabb–Foster fits. The irreversible traps are saturated by the pre-conditioning protocol and do not contribute to the analysed transients (Section 2.6).

P_{H_2} (bar)	E_b (kJ mol^{-1})	N_r (cm^{-3})	k_r (cm^3 s^{-1})	p (s^{-1})
Johnson Global Fit				
–	59.3	$1.17 \cdot 10^{17}$	–	–
Global McNabb–Foster Fit				
–	62.7	$9.41 \cdot 10^{16}$	$5.41 \cdot 10^{-16}$	$1.87 \cdot 10^{-3}$
Individual McNabb–Foster Fits				
0.01	57.9	$1.40 \cdot 10^{17}$	$1.82 \cdot 10^{-15}$	0.0445
0.08	55.6	$5.10 \cdot 10^{16}$	$1.67 \cdot 10^{-14}$	1.03
0.23	54.2	$4.89 \cdot 10^{16}$	$1.37 \cdot 10^{-14}$	1.52
0.35	61.7	$9.24 \cdot 10^{16}$	$4.00 \cdot 10^{-16}$	$2.11 \cdot 10^{-3}$
0.53	53.2	$1.55 \cdot 10^{17}$	$7.99 \cdot 10^{-16}$	0.134
1.00	51.9	$8.52 \cdot 10^{16}$	$5.82 \cdot 10^{-15}$	1.67

still scatter across pressures, as expected for an ill-conditioned single-curve inverse problem. The per-curve reversible trap density N_r ranges from $4.89 \cdot 10^{16}$ cm^{-3} at 0.23 bar to $1.55 \cdot 10^{17}$ cm^{-3} at 0.53 bar—a factor of ~ 3 for a quantity that should be a material constant at fixed temperature. Notably, the Johnson global estimate $N_r = 1.17 \cdot 10^{17}$ cm^{-3} falls within this scatter band, providing cross-consistency between the two frameworks despite the per-curve variance. This residual drift is a known consequence of fitting individual curves in isolation: the ill-conditioned parameter landscape lets the identified parameters drift across pressures even when the underlying physics is the same, because measurement noise projects onto correlated directions in parameter space [32,33,35]. It underlines that good curve reproduction does not by itself guarantee uniquely identifiable parameters, and that multi-pressure analytical fits (such as the Johnson model) are preferable for extracting physical constants. The per-curve binding energies average to 55.8 kJ mol^{-1}, ranging from 51.9 to 61.7 kJ mol^{-1} across the 6 pressures; the mean is consistent with the Johnson global estimate and with permeation-derived trap binding energies reported for ferrite [28,32].

3.3.2. Global McNabb–Foster fit

Section 2.6 noted that a global multi-pressure MF fit is a higher-dimensional and more severely ill-conditioned optimisation problem than the analytical Johnson global fit, and is computationally far more costly than either the Johnson fit or a single per-curve MF fit. We nonetheless carried it out, because it provides a direct, model-consistent cross-check of the Johnson global result within the McNabb–Foster framework itself. The dimensionless groupings (λ, μ, ρ) are fitted jointly to all six transients, with ρ (and hence C_0) scaled across pressures via the Sieverts relation of Eq. (1), so that the fit has effectively three free physical unknowns (N_r, k_r, p) rather than three per curve. The two-stage Bayesian/Nelder–Mead optimiser of Section 2.6 is applied to the summed residual over all six curves. Fig. 9 shows the resulting global-fit overlays. The fit recovers $N_r = 9.41 \cdot 10^{16}$ cm^{-3} and a binding energy E_b = 62.7 kJ mol^{-1}, in close agreement with both the Johnson global estimate ($N_r = 1.17 \cdot 10^{17}$ cm^{-3}, E_b = 59.3 kJ mol^{-1}) and the per-curve MF range reported above, and within the literature range for cold-rolled iron [28,32]. The summed normalised-flux RMS residual of the global fit (0.0499) is larger than the per-curve mean (0.0124) or maximum (0.0184) RMS, as expected: forcing a single trap-parameter set to reproduce all six transients trades per-curve fit quality for a physically constrained, materially consistent parameter set. Visually (Fig. 9), the global fit reproduces the sub-atmospheric transients closely but systematically leads the data at the highest pressures (0.53 and 1.00 bar)—the same near-saturation regime identified as the source of the largest Johnson residual in Section 3.2—which is consistent with a single reversible-trap population becoming a progressively less

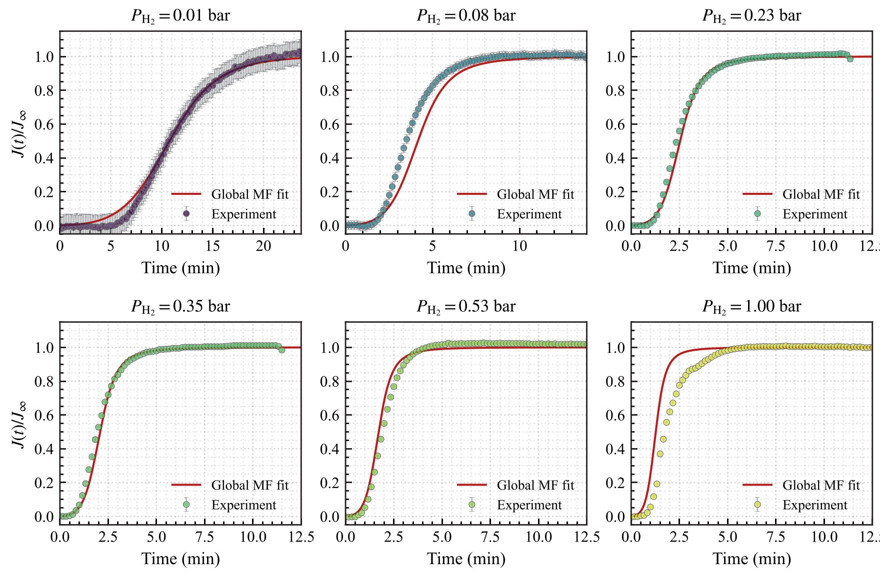

Fig. 9. Global McNabb–Foster inverse-fit overlays for the six ARMCO iron transients (cold-rolled ARMCO iron, $L = 0.012$ cm, $T = 20$ °C), sharing one reversible-trap parameter set ($N_r = 9.41 \cdot 10^{16}$ cm^{-3}, $E_b = 62.7$ kJ mol^{-1}) across all pressures. Filled circles: experimental normalised flux. Solid line: global MF fit.

complete description as trap occupancy approaches saturation. Taken together, the global MF fit corroborates the Johnson global result from within an independent numerical framework, while the per-curve fits above remain the clearest illustration of the ill-conditioning that motivates preferring multi-pressure global fits (Johnson or MF) over any single-curve inversion.

4. Discussion

4.1. Methodological significance and limitations

The most direct value of the present results is methodological. It is operationally feasible to characterise hydrogen permeation across two decades of H_2 partial pressure in a single apparatus, using only common laboratory hardware: a mass flow controller, an inert carrier line, a standard potentiostat. The decisive enablers are the controlled palladium electroplating procedure of Section 2.1, which makes a highly diffusive ferrite compatible with a catalyst layer that would otherwise blister, and the calibrated mass-flow pressure imposition of Section 2.3, whose imposed partial pressures are independently corroborated by the Sieverts $\sqrt{P_{H_2}}$ flux dependence (Fig. 4). Together these two ingredients show that the sub-atmospheric regime is a natural extension of the Devanathan–Stachurski technique, accessible to any laboratory already equipped for ISO 17081 measurements [30,31].

The wider scientific motivation is the trap-saturation argument set out in the introduction. At 1.00-bar hydrogen activity, the fractional trap occupancy $n = \beta/(1+\beta)$ approaches unity [12,32] and the Johnson formula of Eq. (5) is poorly conditioned: at large β, small simultaneous adjustments of α and β_1 leave the time-lag ratio nearly unchanged, so inverting the formula for the two trap parameters separately is mathematically ill-conditioned and requires strong priors that bias the inferred binding energies and trap densities [33]. At sub-atmospheric activity, by contrast, β is reduced (scaling as $\sqrt{P_{H_2}}$ via the Sieverts inlet condition) and the sensitivity of t_T/t_L to α and β_1 individually becomes sufficient for well-conditioned joint identification. The global fit of Fig. 7 across two decades of partial pressure provides empirical support for this argument on a real ferrite.

Several constraints of the present implementation require explicit acknowledgement.

1. The H_2 partial pressure is imposed by calibrated mass-flow control, so its accuracy rests on the flowmeter calibration. The steady-state flux provides an independent cross-check through the Sieverts $\sqrt{P_{H_2}}$ dependence (Eq. (3), Fig. 4), which the data follow closely; this consistency relies on the inlet remaining a Sieverts equilibrium across the explored range, supported by the palladium catalyst layer that ensures rapid dissociative adsorption and thermodynamic equilibrium between the gas phase and the subsurface lattice.
2. All experiments are conducted at a single temperature ($T = 20$ °C $= 293$ K), so no Arrhenius decomposition of D_L or K_S into activation prefactors is attempted.
3. The solubility of hydrogen in the matrix is not directly measured; only the product $D_L K_S$ enters the permeation flux, and separating the lattice diffusivity from the solubility requires either an independent diffusivity measurement [29,44,52,53] or a complementary thermal desorption analysis [37,54], or the literature assumptions we have made.
4. The analytical Johnson formula rests on three assumptions whose approximate character should be made explicit, since each can bias the fitted trap parameters.

    (a) *Local equilibrium* between lattice and trapped hydrogen [19,46] requires trap capture/release kinetics to be fast relative to the diffusive time scale; this degrades as the reversible-trap population approaches saturation, where release becomes comparatively rate-limiting.
    (b) A *single reversible-trap population* with one binding energy is assumed; a material with a distributed trap-energy spectrum [16,21] deviates most from this idealisation where trap occupancy is highest, since a spread of energies collapses toward a single effective value only in the low-occupancy limit.
    (c) The *lattice diffusivity* D_L is fixed at its literature value (Section 2.4) rather than fitted, because D_L and the trap parameters are degenerate in single-curve time-lag fitting [33]; fixing D_L removes a degree of freedom that could otherwise absorb part of the near-saturation curvature, so a genuine mismatch between the assumed and true D_L would appear as residual structure rather than being compensated.

The residual analysis of Fig. 7 bears this out: the largest relative deviation falls at the highest, near-saturation pressure rather than at the lowest, so the global $R^2 = 0.919$ reflects the approximate character of these assumptions where trap occupancy is highest.

5. Each pressure was measured in a single permeation run (Section 2.5); the reported uncertainties therefore reflect instrument-propagated error rather than run-to-run reproducibility, and repeated measurements at fixed pressure remain an item for future work.

4.2. Implications for hydrogen-embrittlement standards

The international standards for hydrogen permeation measurement [30,31] prescribe an electrochemical cathodic-charging protocol that, in current practice, operates at hydrogen activities close to or higher than H_2 at atmospheric pressure. At these activities the reversible-trap population is nearly saturated, so the Johnson inversion is poorly conditioned and the resulting trap parameters carry large uncertainty. The data presented here show that a hybrid gas-inlet/electrochemical-outlet configuration delivers equivalent steady-state and time-lag information across two decades of H_2 partial pressure, with no additional hardware beyond a mass flow controller and an inert carrier line. A sub-atmospheric extension of the existing standards, parameterised by H_2 partial pressure rather than by cathodic charging current density, would substantially improve the conditioning of the trap-parameter identification and thereby extend the analytical information that a single permeation campaign can deliver [12,16,55].

5. Conclusions

Extending Devanathan–Stachurski permeation measurements on cold-rolled ARMCO iron to sub-atmospheric H_2 partial pressures (P_{H_2} = 0.01 to 1.00 bar) resolves the ill-conditioning that limits trap-parameter identification at near-atmospheric hydrogen activity. The Johnson two-parameter time-lag formula, fitted jointly across all 6 measured pressures with the lattice diffusivity held at its literature value, recovers $\alpha = 8.55 \cdot 10^3$ and $\beta_1 = 91.1$ with a log-time $R^2 = 0.919$, yielding a model-derived effective binding energy $E_b = 59.3\ \mathrm{kJ\,mol^{-1}}$ (68% MC CI: 59.0–59.7 $\mathrm{kJ\,mol^{-1}}$) and a reversible-trap density $N_r = 1.17 \cdot 10^{17}\ \mathrm{cm^{-3}}$, consistent with literature values for cold-rolled iron [28,32]. Both per-curve and global McNabb–Foster inverse fits cross-validate this result from an independent numerical framework, at the cost of larger parameter scatter in the per-curve case. Future work will extend the technique to systematic temperature scans—enabling a direct Arrhenius determination of the binding energy—and to other ferritic materials with different trap populations.

CRediT authorship contribution statement

Tommaso Grossi: Writing – review & editing, Writing – original draft, Visualization, Validation, Software, Methodology, Investigation, Data curation. **Valentina Colla:** Writing – review & editing, Supervision, Software, Project administration, Data curation. **Fernanda Di Giorgio:** Writing – review & editing, Methodology, Investigation, Formal analysis, Conceptualization. **Renzo Valentini:** Writing – review & editing, Supervision, Resources, Project administration, Funding acquisition, Conceptualization.

Declaration of competing interest

The authors declare that they have no known competing financial interests or personal relationships that could have appeared to influence the work reported in this paper.

Appendix. Derivation of the Johnson time-lag formula

Governing equation under local equilibrium. Assume a single reversible trap population in instantaneous equilibrium with the lattice, so that the fractional occupancy satisfies the Langmuir isotherm [56]

$$\theta_r(x,t) = \frac{k_r C(x,t)/p}{1 + k_r C(x,t)/p} = \frac{\beta\chi}{1+\beta\chi}, \tag{13}$$

where $\chi = C/C_0$ is the dimensionless lattice concentration, $\beta = k_r C_0/p$ is the trap-occupancy parameter at the inlet surface, and $\alpha = N_r k_r/p$ is the trap-strength parameter. Substituting into the mass balance $\partial_t(C + N_r\theta_r) = D_L\,\partial_x^2 C$ and using the dimensionless variables $X = x/L$, $\tau = D_L t/L^2$ gives

$$\frac{\partial \xi}{\partial \tau} = \frac{\partial^2 \chi}{\partial X^2}, \qquad \xi(\chi) \equiv \chi + \frac{\alpha\chi}{1+\beta\chi}. \tag{14}$$

At steady state the right-hand side vanishes, so $\chi_{ss}(X) = 1 - X$ (linear profile), and the dimensionless steady-state flux is $-\partial\chi_{ss}/\partial X|_1 = 1$.

Loading transient (inlet stepped from 0 to C_0). For this case, we have the boundary and initial conditions $\chi(0,\tau) = 1$, $\chi(1,\tau) = 0$, and $\chi(X,0) = 0$. Operationally, the loading time lag t_T is defined as the intercept on the time axis of the steady-state linear asymptote of the cumulative permeation $Q(t) = \int_0^t J(t')\,dt'$ as $t \to \infty$. Since at long times this asymptote is $Q(t) \sim J_\infty(t - t_T)$, the quantity of hydrogen accumulated in the membrane to establish the steady-state profile equals $J_\infty t_T$. Geometrically, this quantity corresponds to the difference between the ideal cumulative permeation without transient delay ($J_\infty t$) and the actual cumulative permeation $Q(t)$ as $t \to \infty$:

$$J_\infty t_T = \int_0^\infty \left[J_\infty - J(t)\right] dt. \tag{15}$$

The integrand $J_\infty - J(t)$ decays exponentially at long times (each eigenmode of the nonlinear diffusion operator contributes a decaying exponential), so the integral converges and the time-axis intercept is well-defined. Expressed in dimensionless variables using the exit flux ratio

$$\frac{J(t)}{J_\infty} = -\left.\frac{\partial\chi}{\partial X}\right|_{X=1} \tag{16}$$

and $dt = (L^2/D_L)\,d\tau$, the dimensionless loading time lag is

$$\tau_T^{(l)} = \int_0^\infty \left[1 + \left.\frac{\partial\chi}{\partial X}\right|_{X=1}\right] d\tau. \tag{17}$$

Multiply Eq. (14) by X and integrate over $[0,1]$; integration by parts on the right-hand side gives

$$\int_0^1 X\frac{\partial\xi}{\partial\tau}\,dX = \left.\frac{\partial\chi}{\partial X}\right|_{X=1} + 1, \tag{18}$$

using $\chi(0,\tau) = 1$ and $\chi(1,\tau) = 0$. Integrating Eq. (18) over $\tau \in [0,\infty)$, the left-hand side collapses to a spatial integral over the change from the initial to the final ($\tau \to \infty$) state of ξ:

$$\tau_T^{(l)} = \int_0^1 X\left[\xi(\chi_{ss}(X)) - \xi(0)\right] dX = \int_0^1 X\,\xi(1-X)\,dX. \tag{19}$$

Unloading transient (inlet stepped from C_0 to 0). For this case, we have the boundary and initial conditions $\chi(0,\tau) = 0$, $\chi(1,\tau) = 0$, and $\chi(X,0) = \chi_{ss}(X) = 1 - X$. Operationally, the unloading time lag $t_T^{(d)}$ is defined as the intercept on the time axis of the steady-state linear asymptote of the cumulative exit-flux deficit $\bar{Q}(t) = \int_0^t \left[J_\infty - J(t')\right] dt'$. As the membrane empties completely, $J(t) \to 0$, so the cumulative deficit approaches the linear asymptote $\bar{Q}(t) \sim J_\infty t - \int_0^\infty J(t')\,dt' = J_\infty(t - t_T^{(d)})$. This directly yields:

$$t_T^{(d)} = \frac{1}{J_\infty}\int_0^\infty J(t)\,dt. \tag{20}$$

Expressed in dimensionless variables using the exit flux ratio

$$\frac{J(t)}{J_\infty} = -\left.\frac{\partial\chi}{\partial X}\right|_{X=1} \tag{21}$$

and $\mathrm{d}t = (L^2/D_L)\,\mathrm{d}\tau$, the dimensionless unloading time lag is

$$\tau_T^{(d)} = \int_0^\infty \left(-\frac{\partial \chi}{\partial X}\Big|_{X=1} \right) \mathrm{d}\tau. \tag{22}$$

With both boundary values now zero, the same moment operation $\int_0^1 X\,(\cdot)\,\mathrm{d}X$ on Eq. (14) gives

$$\int_0^1 X \frac{\partial \xi}{\partial \tau}\,\mathrm{d}X = \frac{\partial \chi}{\partial X}\Big|_{X=1}. \tag{23}$$

Integrating over $\tau \in [0, \infty)$: the initial state at $\tau = 0$ is $\xi(1 - X)$ (the loaded steady-state profile), and the final state at $\tau \to \infty$ is $\xi(\chi{=}0) = 0$ (empty membrane). Therefore:

$$\tau_T^{(d)} = \int_0^1 X\,\xi(1 - X)\,\mathrm{d}X = \tau_T^{(l)}. \tag{24}$$

The loading and unloading time lags are therefore identical: both equal the same spatial integral of ξ over the steady-state profile.

Evaluation of the integral. Setting $v = 1 - X$ in Eq. (19):

$$\tau_T = \int_0^1 (1 - v)\,\xi(v)\,\mathrm{d}v = \underbrace{\int_0^1 (1 - v) v\,\mathrm{d}v}_{=1/6} + \alpha \int_0^1 \frac{(1 - v)\,v}{1 + \beta v}\,\mathrm{d}v. \tag{25}$$

The first term is the Fickian lag $\tau_L = 1/6$. For the second integral, substituting $w = \beta v$ and splitting the numerator:

$$\int_0^1 \frac{v}{1 + \beta v}\,\mathrm{d}v = \frac{1}{\beta^2}\left[\beta - \ln(1 + \beta)\right], \tag{26}$$

$$\int_0^1 \frac{v^2}{1 + \beta v}\,\mathrm{d}v = \frac{1}{\beta^3}\left[\frac{\beta^2}{2} - \beta + \ln(1 + \beta)\right]. \tag{27}$$

Subtracting Eq. (27) from Eq. (26) and simplifying:

$$\int_0^1 \frac{(1 - v)v}{1 + \beta v}\,\mathrm{d}v = \frac{1}{2\beta} + \frac{1}{\beta^2} - \frac{1}{\beta^3}(1 + \beta)\ln(1 + \beta). \tag{28}$$

Inserting into Eq. (25) and dividing by $\tau_L = 1/6$:

$$\frac{t_T}{t_L} = 1 + \frac{3\alpha}{\beta} + \frac{6\alpha}{\beta^2} - \frac{6\alpha}{\beta^3}(1 + \beta)\ln(1 + \beta), \tag{29}$$

which is Eq. (5). The same expression applies to the unloading time lag $t_T^{(d)}$, with the identification that β is evaluated at the pre-switch inlet concentration C_0 and the time lag is measured through the integral of the decay current (Eq. (22)) rather than as the intercept of the cumulative permeation asymptote.

References

[1] Hirth JP. Effects of hydrogen on the properties of iron and steel. Met Trans A 1980;11(6):861–90. http://dx.doi.org/10.1007/BF02654700.

[2] Nagumo M. Fundamentals of hydrogen embrittlement. Singapore: Springer; 2016, http://dx.doi.org/10.1007/978-981-10-0161-1.

[3] Lynch S. Hydrogen embrittlement phenomena and mechanisms. Corros Rev 2012;30(3–4):105–23. http://dx.doi.org/10.1515/corrrev-2012-0502.

[4] Robertson IM, Sofronis P, Nagao A, Martin ML, Wang S, Gross DW, Nygren KE. Hydrogen embrittlement understood. Met Mater Trans B 2015;46(3):1085–103. http://dx.doi.org/10.1007/s11663-015-0325-y.

[5] Birnbaum HK, Sofronis P. Hydrogen-enhanced localized plasticity—a mechanism for hydrogen-related fracture. Mater Sci Eng: A 1994;176(1–2):191–202. http://dx.doi.org/10.1016/0921-5093(94)90975-X.

[6] Sofronis P, McMeeking RM. Numerical analysis of hydrogen transport near a blunting crack tip. J Mech Phys Solids 1989;37(3):317–50. http://dx.doi.org/10.1016/0022-5096(89)90002-1.

[7] Robertson IM, Birnbaum HK, Sofronis P. Chapter 91 hydrogen effects on plasticity. Elsevier; 2009, p. 249–93. http://dx.doi.org/10.1016/S1572-4859(09)01504-6.

[8] Martin ML, Dadfarnia M, Nagao A, Wang S, Sofronis P. Enumeration of the hydrogen-enhanced localized plasticity mechanism for hydrogen embrittlement in structural materials. Acta Mater 2019;165:734–50. http://dx.doi.org/10.1016/j.actamat.2018.12.014.

[9] Nagumo M, Takai K. The predominant role of strain-induced vacancies in hydrogen embrittlement of steels: Overview. Acta Mater 2019;165:722–33. http://dx.doi.org/10.1016/j.actamat.2018.12.013.

[10] Devanathan MAV, Stachurski Z. The adsorption and diffusion of electrolytic hydrogen in palladium. Proc R Soc Lond Ser A. Math Phys Sci 1962;270(1340):90–102. http://dx.doi.org/10.1098/rspa.1962.0205.

[11] Devanathan MAV, Stachurski Z, Beck W. A technique for the evaluation of hydrogen embrittlement characteristics of electroplating baths. J Electrochem Soc 1963;110(8):886. http://dx.doi.org/10.1149/1.2425894.

[12] Bhadeshia HKDH. Prevention of hydrogen embrittlement in steels. ISIJ Int 2016;56(1):24–36. http://dx.doi.org/10.2355/isijinternational.ISIJINT-2015-430.

[13] Lovicu G, Bottazzi M, D'Aiuto F, De Sanctis M, Dimatteo A, Santus C, Valentini R. Hydrogen embrittlement of automotive advanced high-strength steels. Met Mater Trans A 2012;43(11):4075–87. http://dx.doi.org/10.1007/s11661-012-1280-8.

[14] Li X, Ma X, Zhang J, Akiyama E, Wang Y, Song X. Review of hydrogen embrittlement in metals: Hydrogen diffusion, hydrogen characterization, hydrogen embrittlement mechanism and prevention. Acta Met Sin (Engl Lett) 2020;33(6):759–73. http://dx.doi.org/10.1007/s40195-020-01039-7.

[15] Aiello F, Beghini M, Belardini CM, Bertini L, Macoretta G, Monelli BD, Valentini R. Proposal of a hydrogen embrittlement index for a martensitic advanced high-strength steel. Corros Sci 2023;222:111357. http://dx.doi.org/10.1016/j.corsci.2023.111357.

[16] Turnbull A. Perspectives on hydrogen uptake, diffusion and trapping. Int J Hydrog Energy 2015;40(47):16961–70. http://dx.doi.org/10.1016/j.ijhydene.2015.06.147.

[17] Yamabe J, Awane T, Matsuoka S. Investigation of hydrogen transport behavior of various low-alloy steels with high-pressure hydrogen gas. Int J Hydrog Energy 2015;40(34):11075–86. http://dx.doi.org/10.1016/j.ijhydene.2015.07.006.

[18] Yamabe J, Yoshikawa M, Matsunaga H, Matsuoka S. Hydrogen trapping and fatigue crack growth property of low-carbon steel in hydrogen-gas environment. Int J Fatigue 2017;102:202–13. http://dx.doi.org/10.1016/j.ijfatigue.2017.04.010.

[19] Oriani RA. The diffusion and trapping of hydrogen in steel. Acta Metall 1970;18(1):147–57. http://dx.doi.org/10.1016/0001-6160(70)90078-7.

[20] McNabb A, Foster PK. A new analysis of the diffusion of hydrogen in iron and ferritic steels. Institute of Metals Division, AIME; 1963.

[21] Kirchheim R. Hydrogen solubility and diffusivity in defective and amorphous metals. Prog Mater Sci 1988;32(4):261–325. http://dx.doi.org/10.1016/0079-6425(88)90010-2.

[22] Pundt A, Kirchheim R. Hydrogen in metals: Microstructural aspects. Annu Rev Mater Res 2006;36(1):555–608. http://dx.doi.org/10.1146/annurev.matsci.36.090804.094451.

[23] Wipf H. Diffusion of hydrogen in metals. Springer; 1997, p. 51–91. http://dx.doi.org/10.1007/BFb0103401.

[24] Iino M. Analysis of irreversible hydrogen trapping. Acta Metall 1982;30(2):377–83. http://dx.doi.org/10.1016/0001-6160(82)90217-6.

[25] Iino M. Trapping of hydrogen by sulfur-associated defects in steel. Met Trans A 1985;16(3):401–9. http://dx.doi.org/10.1007/BF02814338.

[26] Pressouyre GM. Trap theory of Hydrogen embrittlement. Acta Metall 1980;28(7):895–911. http://dx.doi.org/10.1016/0001-6160(80)90106-6.

[27] Pressouyre GM, Bernstein IM. An example of the effect of hydrogen trapping on hydrogen embrittlement. Met Trans A 1981;12(5):835–44. http://dx.doi.org/10.1007/BF02648348.

[28] Kumnick AJ, Johnson HH. Deep trapping states for hydrogen in deformed iron. Acta Metall 1980;28(1):33–9. http://dx.doi.org/10.1016/0001-6160(80)90038-3.

[29] Kiuchi K, McLellan RB. The solubility and diffusivity of hydrogen in well-annealed and deformed iron. Acta Metall 1983;31(7):961–84. http://dx.doi.org/10.1016/0001-6160(83)90192-X.

[30] International Organization for Standardization. ISO 17081:2014 - Method of measurement of hydrogen permeation and determination of hydrogen uptake and transport in metals by an electrochemical technique. Technical report, Geneva, Switzerland: ISO; 2014.

[31] Standard ASTM. G148-97 Standard practice for evaluation of hydrogen uptake, permeation, and transport in metals by an electrochemical technique. Technical report, West Conshohocken, PA: ASTM International; 2018.

[32] Johnson HH. Hydrogen in iron. Met Trans A 1988;19(10):2371–87. http://dx.doi.org/10.1007/BF02645465.

[33] Castaño-Rivera P, Ramunni VP, Bruzzoni P. Numerical study of hydrogen trapping: Application to an API 5L X60 steel. ISRN Mater Sci 2012;2012:1–14. http://dx.doi.org/10.5402/2012/945235.

[34] Nelson HG, Stein JE. Gas-Phase hydrogen permeation through alpha iron, 4130 steel, and 304 stainless steel from less than 100 C to near 600 C. Technical report, NASA Ames Research Center; 1973.

[35] Johnson HH. Environment and fracture: Progress report. Progress report, Ithaca, N.Y.: Department of Materials Science and Engineering, Cornell University; 1981.

[36] Szkodo M, Chodnicka-Wszelak K, Deja M, Stanisławska A, Bartmański M. The influence of the depth of cut in single-pass grinding on the microstructure and properties of the C45 steel surface layer. Materials 2020;13(5):1040. http://dx.doi.org/10.3390/ma13051040.

[37] Choo WY, Lee JY. Thermal analysis of trapped hydrogen in pure iron. Met Trans A 1982;13(1):135–40. http://dx.doi.org/10.1007/BF02642424.

[38] Boes N, Züchner H. Electrochemical methods for studying diffusion, permeation and solubility of hydrogen in metals. J Less Common Met 1976;49:223–40. http://dx.doi.org/10.1016/0022-5088(76)90037-0.

[39] Manolatos P, Jerome M, Galland J. Necessity of a palladium coating to ensure hydrogen oxidation during electrochemical permeation measurements on iron. Electrochim Acta 1995;40(7):867–71. http://dx.doi.org/10.1016/0013-4686(94)00343-Y.

[40] Manolatos P, Jerome M. A thin palladium coating on iron for hydrogen permeation studies. Electrochim Acta 1996;41(3):359–65. http://dx.doi.org/10.1016/0013-4686(95)00379-7.

[41] Fuller EN, Schettler PD, Giddings J Calvin. New method for prediction of binary gas-phase diffusion coefficients. Ind Eng Chem 1966;58(5):18–27. http://dx.doi.org/10.1021/ie50677a007.

[42] Daynes HA. The process of diffusion through a rubber membrane. Proc R Soc Lond Ser A, Contain Pap A Math Phys Character 1920;97(685):286–307. http://dx.doi.org/10.1098/rspa.1920.0034.

[43] Frisch HL. The time lag in diffusion. J Phys Chem 1957;61(1):93–5. http://dx.doi.org/10.1021/j150547a018.

[44] Hagi H, Hayashi Y, Ohtani N. Diffusion coefficient of hydrogen in pure iron between 230 and 300 K. Trans Japan Inst Met 1979;20(7):349–57. http://dx.doi.org/10.2320/matertrans1960.20.349.

[45] Virtanen P, Gommers R, Oliphant TE, Haberland M, Reddy T, Cournapeau D, et al. SciPy 1.0: Fundamental algorithms for scientific computing in Python. Nature Methods 2020;17(3):261–72. http://dx.doi.org/10.1038/s41592-019-0686-2.

[46] Krom AHM, Bakker A. Hydrogen trapping models in steel. Met Mater Trans B 2000;31(6):1475–82. http://dx.doi.org/10.1007/s11663-000-0032-0.

[47] Krom AHM, Koers RWJ, Bakker A. Hydrogen transport near a blunting crack tip. J Mech Phys Solids 1999;47(4):971–92. http://dx.doi.org/10.1016/S0022-5096(98)00064-7.

[48] Toribio J, Kharin V. A generalised model of hydrogen diffusion in metals with multiple trap types. Phil Mag 2015;95(31):3429–51. http://dx.doi.org/10.1080/14786435.2015.1079660.

[49] Bergstra J, Bardenet R, Bengio Y, Kégl B. Algorithms for hyper-parameter optimization. In: Advances in neural information processing systems, vol. 24, Curran Associates, Inc.; 2011.

[50] Akiba T, Sano S, Yanase T, Ohta T, Koyama M. Optuna. ACM; 2019, p. 2623–31. http://dx.doi.org/10.1145/3292500.3330701.

[51] Nelder JA, Mead R. A simplex method for function minimization. Comput J 1965;7(4):308–13. http://dx.doi.org/10.1093/comjnl/7.4.308.

[52] Da Silva JRG, Stafford SW, McLellan RB. The thermodynamics of the hydrogen-iron system. J Less Common Met 1976;49:407–20. http://dx.doi.org/10.1016/0022-5088(76)90052-7.

[53] Quick NR, Johnson HH. Hydrogen and deuterium in iron, 49–506°C. Acta Metall 1978;26(6):903–7. http://dx.doi.org/10.1016/0001-6160(78)90041-X.

[54] Verbeken K. Analysing hydrogen in metals: bulk thermal desorption spectroscopy (TDS) methods. Elsevier; 2012, p. 27–55. http://dx.doi.org/10.1533/9780857095374.1.27.

[55] Campari A, Ustolin F, Alvaro A, Paltrinieri N. A review on hydrogen embrittlement and risk-based inspection of hydrogen technologies. Int J Hydrog Energy 2023;48(90):35316–46. http://dx.doi.org/10.1016/j.ijhydene.2023.05.293.

[56] Langmuir I. The adsorption of gases on plane surfaces of glass, mica and platinum. J Am Chem Soc 1918;40(9):1361–403. http://dx.doi.org/10.1021/ja02242a004.